RESEARCH ARTICLE | JANUARY 22 2026

Writing metasurfaces by hand: A pen-based MXene approach for flexible and low-waste paper platforms

William O. F. Carvalho ; Murilo H. M. Facure ; Luciano Leonel Mendes ; Osvaldo N. Oliveira, Jr. ; Daniel S. Correa ; Jorge Ricardo Mejía-Salazar

J. Appl. Phys. 139, 045302 (2026)
https://doi.org/10.1063/5.0306436

Journal of Applied Physics ARTICLE pubs.aip.org/aip/jap

Writing metasurfaces by hand: A pen-based MXene approach for flexible and low-waste paper platforms

Cite as: J. Appl. Phys. **139**, 045302 (2026); doi: 10.1063/5.0306436
Submitted: 10 October 2025 · Accepted: 2 January 2026 ·
Published Online: 22 January 2026

William O. F. Carvalho,[1,a)] Murilo H. M. Facure,[2] Luciano Leonel Mendes,[1] Osvaldo N. Oliveira, Jr.,[3] Daniel S. Correa,[4] and Jorge Ricardo Mejía-Salazar[1]

AFFILIATIONS

[1]National Institute of Telecommunications (Inatel), Santa Rita do Sapucaí, MG 37536-001, Brazil
[2]Department of Materials Engineering, São Carlos School of Engineering, University of Sao Paulo, São Carlos, SP 13563-120, Brazil
[3]Sao Carlos Institute of Physics, University of Sao Paulo, São Carlos, SP 13560-970, Brazil
[4]Nanotechnology National Laboratory for Agriculture (LNNA), Embrapa Instrumentação, São Carlos, SP 13560-970, Brazil

[a)]**Author to whom correspondence should be addressed:** william.orivaldo@inatel.br

ABSTRACT

The integration of flexibility, electrical conductivity, and cost-effectiveness remains a central challenge in the fabrication of metasurfaces for electromagnetic applications. Here, we introduce a hybrid pen-based and mask-assisted fabrication strategy for $Ti_3C_2T_x$ MXene-based metasurfaces on paper substrates, enabling precise patterning with minimal material waste. The approach combines screen-printing-derived adhesive masks with a direct ink writing process using MXene inks, yielding conformable and conductive metasurfaces that operate efficiently across the microwave range. Atomic force microscopy and scanning electron microscopy analyses confirmed the formation of uniform, ultra-smooth MXene films (root-mean-square roughness ≈ 438 pm, with a thickness of $\approx 13\,\mu$m) atop paper layers with a total device thickness of 163.6 μm. Experimental transmission spectra revealed strong stopband resonances for metasurfaces based on square-ring and split-ring resonators, with reflection dips near -12 dB. These results are consistent with finite-element method simulations performed using COMSOL Multiphysics, confirming the consistency between numerical predictions and laboratory measurements. The main limitation we observed was the moderate conductivity of our prepared MXene films (8.97×10^3 S/m), which can be enhanced through ink optimization. The low-cost, scalable, and sustainable MXene patterning shown in this work opens new opportunities for fabricating lightweight, flexible, and reconfigurable electromagnetic devices, particularly in wearable and next-generation wireless communication systems.

I. INTRODUCTION

Metasurfaces, first demonstrated nearly three decades ago,[1,2] have since become a cornerstone of modern photonics. Unlike conventional metamaterials that rely on bulky three-dimensional arrays of subwavelength resonators, metasurfaces employ carefully engineered two-dimensional unit cells to control electromagnetic responses. Their ultrathin architecture, often less than one-quarter of the operating wavelength ($d \leq \lambda/4$), enables compact integration and has revolutionized the performance of optical and microwave devices.[3–6] This unique combination of planar geometry and electromagnetic tunability allows metasurfaces to manipulate electromagnetic (EM) waves with unprecedented precision, providing control over amplitude, phase, polarization, and wavefront shaping.[7–9] As a result, metasurfaces have found extensive applications in advanced antennas,[10,11] biosensors,[12–14] absorbers,[15] and wearable technologies.[16]

Metasurfaces may exhibit bandpass, low-pass, high-pass, and stopband functionalities, broadly explored as compact platforms capable of tailoring electromagnetic propagation through engineered resonant responses.[17] Among these categories, stopband metasurfaces are particularly attractive because their resonant unit cells [such as split-ring resonators (SRRs) and square-ring

resonators (SqRRs)] enable the sharp rejection of specific frequency bands, making them suitable for filtering, shielding, and sensing applications.[18,19] While substantial progress has been made in designing resonant inclusions that enhance stopband selectivity, angular stability, or bandwidth, most existing implementations continue to rely on rigid or semi-rigid substrates and fixed geometries, which restrict their use in mechanically demanding or conformal environments. This reliance on non-flexible platforms not only limits the conformability of the metasurfaces but also constrains their integration into flexible, deformable, or sensor-embedded wearable systems, in which stable electromagnetic performance must be preserved even under bending, stretching, or motion.

To address these limitations, recent efforts have focused on developing flexible metasurfaces using polymeric substrates such as polydimethylsiloxane (PDMS), polyethylene terephthalate (PET), poly(methyl methacrylate) (PMMA), and even paper.[20–23] Although these advances represent important progress toward mechanically adaptable metasurfaces, existing fabrication strategies still face considerable challenges. In particular, most rely on sophisticated deposition techniques or metallic inks to form highly conductive resonant unit cells. However, metallic inks suffer from inherent drawbacks, namely, high density and viscosity, that demand specific application methods, often leading to material waste and defects during mask removal in screen-printing processes. In this context, MXenes, a family of two-dimensional transition metal carbides and nitrides with metallic conductivity and mechanical flexibility,[24,25] are a promising alternative. Over the last few years, MXenes have demonstrated exceptional performance in electronics,[26,27] photonics,[28] energy storage,[29] catalysis,[30] chemical sensing,[31] and electromagnetic interference (EMI) shielding.[32] Particularly relevant for flexible metasurfaces, MXenes exhibit excellent adhesion to paper-based substrates when processed in liquid-phase form,[33] enabling scalable, low-cost fabrication through spray-coating, inkjet printing, dipping, and screen printing.[34,35] Despite these advantages, these methods are still limited in terms of material waste and patterning precision when used to fabricate metasurfaces.[24,36,37]

Building upon recent developments in electrochemical sensing and energy storage, where MXene inks have been successfully applied through pen-based direct ink writing (DIW) approaches,[38] we introduce here a novel hybrid strategy for the fabrication of paper-based metasurfaces. Our method combines a screen-printing-derived masking step, used to define precise two-dimensional patterns, with a pen-like direct ink writing process that deposits MXene conductive traces directly onto the substrate. Specifically, the direct deposition of $Ti_3C_2T_x$ MXene ink using a controlled pen-like pipet enables excellent solution-based patterning while remaining fully compatible with flexible and low-cost substrates. This hybrid approach simultaneously eliminates material waste common in conventional screen-printing methods and prevents structural defects associated with mask removal. As a proof-of-concept, we fabricated metasurfaces based on various unit-cell geometries, such as SqRR and SRR, both exhibiting strong stopband filtering with pronounced microwave attenuation. All samples show excellent agreement between numerical simulations and experimental measurements. The high fidelity of the MXene nanopatterning was corroborated by atomic force microscopy (AFM) and scanning electron microscopy (SEM), which confirmed the high surface quality, ultra-low roughness, and uniform film thickness of the resulting conductive layers. Owing to their lightweight, flexible, and conformal nature, such MXene-based metasurfaces open clear pathways toward intelligent communication systems, wearable and skin-mounted sensing, and flexible EMI shielding applications, in which adaptable and conductive patterns are required.

II. METHODS

A. MXene ink synthesis

The synthesis of $Ti_3C_2T_x$ MXene Ink was conducted following the procedure in Ref. 39. Commercially available Ti_3AlC_2 MAX phase ($\geq$90%, $\leq$200 μm, Sigma-Aldrich) was used as the precursor material. The etching of the MAX phase and subsequent delamination of the resulting multilayered MXene were performed using hydrofluoric acid (HF, 40%, Vetec), hydrochloric acid (HCl, 36%, Synth), and lithium chloride (LiCl, Synth). In the procedure, 12 mL HCl and 2.4 mL HF were added to 5.6 mL de-ionized water. Subsequently, 1 g of the MAX phase was slowly added to the solution. The system was stirred at 35 °C for 24 h. Centrifuging cycles (3500 rpm for 5 min) were repeated to wash the resulting multilayer MXene until the pH of the supernatant exceeded 6. The delamination of the multilayer MXene was performed by dispersing it in 50 mL of a 0.5 mol/L LiCl solution. The dispersion was kept under stirring at 35 °C for 20 h. To obtain the delaminated MXene, centrifuging cycles (3500 rpm for 5 min) were initially used to remove LiCl, until the supernatant exhibited a darker coloration indicative of MXene, which was then collected. The concentration of the MXene was achieved through centrifuging at 8000 rpm for 10 min, followed by sediment collection and resuspension in de-ionized water.

B. Metasurface design and fabrication

Figure 1(a) illustrates the proposed metasurface, which consists of MXene conductive patterns deposited onto a paper-based substrate. A normally incident microwave interacts with the metasurface, and under resonant conditions, the electromagnetic wave couples efficiently with the subwavelength unit-cell elements. This design was aimed to demonstrate the feasibility of integrating MXene and paper to create low-cost, flexible metasurfaces for microwave applications. To explore the design flexibility and functional potential of this approach, we selected two well-established resonator geometries in the metasurface literature: the SqRR and the SRR. These structures are known for their characteristic stopband filtering behavior, with resonant frequencies that can be tuned by adjusting geometric parameters. This tunability is illustrated here by fabricating two SqRRs with distinct geometries, alongside an SRR, thereby also demonstrating the ability to realize various unit-cell designs using our fabrication method.

As schematized in Fig. 1(b), the metasurfaces were parametrized with the same square lattice with period Λ along the xy-plane, external and internal MXene boundaries as a and b, respectively, which determine the MXene strip width, and the gap g only for the SRR shape. A step-by-step parametric workflow was

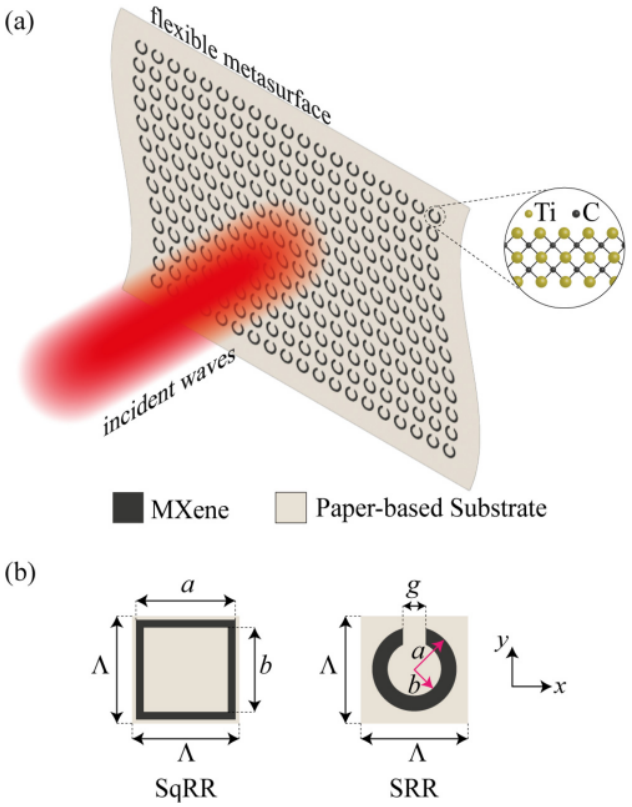

FIG. 1. (a) Schematic illustration of the flexible MXene metasuface and (b) the geometric parameters Λ, *a*, *b*, and *g* for SqRR and SRR unit cells.

then carried out to refine the geometrical parameters of both SqRR and SRR units. First, a coarse sweep of *a*, *b*, and *g* (for SRRs) was performed to identify the approximate regions of strong resonant. Next, a finer parametric optimization was conducted to simultaneously tune the resonance depth and spectral position. The resonant frequencies were determined using full-wave EM simulations through the finite-element method (FEM) in COMSOL Multiphysics®. To consider a two-dimensional infinite periodic structure, Floquet boundary conditions were set along the *xy*-plane. Perfectly matched layers (PMLs) were applied in *z*-boundaries to circumvent undesired reflections. Since our proposal works in microwaves, the results were analyzed in the frequency range of 1–17 GHz under normal incidence. Along with MXene conductivity σ_{MXene} and its thickness t_{MXene}, we considered the paper substrate permittivity as $\varepsilon_s = 1.5$ and thickness $t_s = 75.3\,\mu$m.

Following the numerical design process, the MXene-based flexible metasurfaces were fabricated using a screen-printing method, as illustrated in Fig. 2. Adhesive labels (21 × 29.7 cm, Pimaco), consisting of an offset paper layer bonded to a supporting liner via a removable adhesive (A), were employed as substrates for MXene deposition. This configuration enables the top layer to be peeled off cleanly without leaving adhesive residue on the backing, making it suitable for use as a stencil mask. The metasurface geometries (B), designed in COMSOL Multiphysics, were transferred to a cutting machine (Silhouette Cameo 3) to produce precise screen-printing masks (C). These adhesive masks were cut into the desired patterns corresponding to the metasurface unit cells. The cutting machine provides edge resolutions on the order of several tens of micrometers through a computer-controlled cutting (well above the precision required for microwave unit-cell geometries), ensuring that ink deposition occurs strictly within the defined boundaries. MXene dispersion (D) at a concentration of 1.8 mg/mL was then applied to the masked regions, selectively forming the conductive elements of the metasurface (E). The MXene concentration was systematically tested and adjusted to obtain an appropriate viscosity for DIW deposition, ensuring homogeneous and complete surface coverage. The same predefined volume of MXene ink was dispensed per unit area using a calibrated pipette tip and the DIW motion was constrained by the mask geometry. This method effectively standardizes the lateral spreading of the ink and ensures a consistent film thickness across all samples. After deposition, the samples were allowed to dry at room temperature (approximately 25 °C) (F). Once fully dried, the adhesive mask—now devoid of MXene—was carefully removed (G), leaving behind the patterned conductive structures. The resulting metasurfaces (H) were then ready for electromagnetic characterization. It is worth noting that any lateral spreading of the MXene ink during deposition does not hinder the formation of the desired pattern. The use of the adhesive mask ensures that, after solvent evaporation and complete drying, the subsequent mask removal yields well-defined MXene features exclusively in the intended regions. As a result, the final patterned structures accurately reproduce the designed geometry, as evidenced in the metasurfaces obtained.

We produced flexible metasurfaces for the microwave range, targeting specifically the S-, C-, and K_u-bands. The optimization process aimed to design two distinct SqRR unit cells resonating at $f = 3.5$ GHz and $f = 5.8$ GHz, respectively. For the SRR unit cell, which exhibits broken symmetry, the analysis accounted for both horizontal, *x*-polarization (*x*-pol), and vertical, *y*-polarization (*y*-pol), incident waves. This allowed resonant coupling at different frequencies, specifically $f = 5.8$ GHz for *x*-pol and $f = 14.2$ GHz for *y*-pol. Table I summarizes the optimized geometric parameters used in the numerical simulations.

C. Morphological characterization

The metasurfaces were characterized by atomic force microscopy (AFM) with a Dimension Icon microscope (Bruker) operating in the tapping mode, employing a TESP V2 probe with an oscillation frequency of 330 kHz and a spring constant of 40 N/m, and scanning electron microscopy (SEM) with a JEOL JSM-6510 microscope. The SEM cross-sectional images of the metasurface were obtained by fracturing via immersion in liquid nitrogen to expose the layered structure. The electrical conductivity of the MXene was measured with a resistivity tester by applying a current of 100 mA to the dried MXene surface. The resulting average sheet resistance was $R_{\square} = 8.57\,\Omega/\square$. Determining the conductivity experimentally is essential for incorporating real material parameters into the

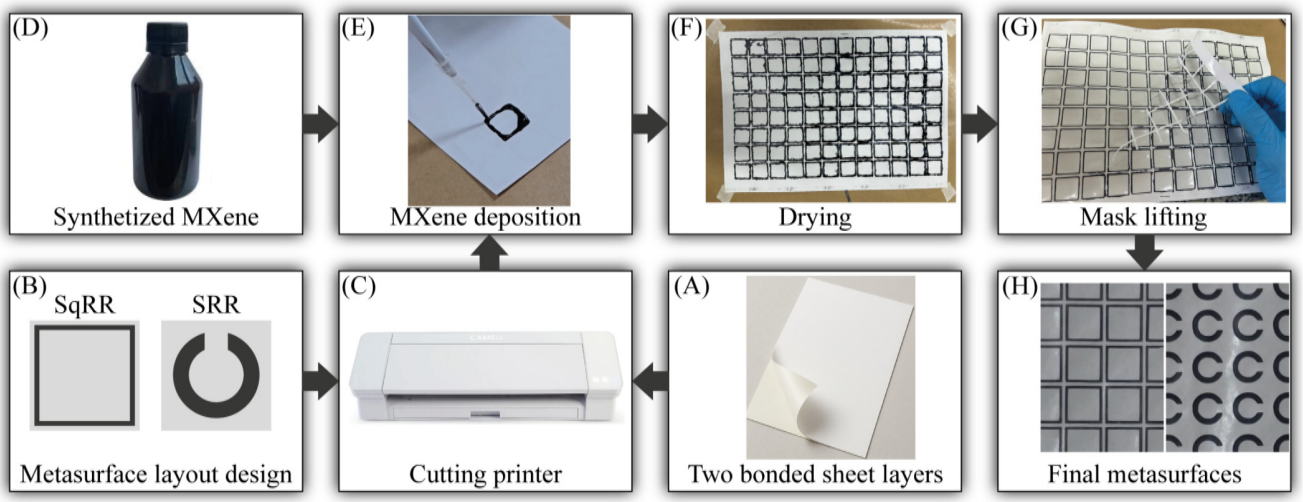

FIG. 2. Fabrication process of MXene-based metasurfaces. (a) Adhesive labels, (b) metasurface designs, (c) cutting printer to produce a screen-printing masks, (d) MXene dispersion, (e) MXene deposition, (f) drying, (g) mask lifting, and (h) resulting metasurfaces.

simulation environment, thereby enhancing the reliability of geometric optimization and numerical results.

III. RESULTS AND DISCUSSION

Figure 3(a) shows an AFM image of the MXene film deposited on the adhesive paper, featuring grain boundaries that indicate the edges of the MXene layers. Due to the 2D morphology of the material, the film also presents a characteristic slightly wrinkled surface. The root-mean-square roughness (R_{rms}) calculated for three film regions was 437.9 ± 44.1 pm, indicating a flat surface. Although AFM characterization is shown for a representative unit cell, additional measurements performed at distinct locations on multiple samples confirmed comparable thickness and conductivity values, indicating that the manual DIW process introduces only minimal variability and does not compromise the electromagnetic performance of the metasurfaces. In the SEM image in Fig. 3(b), three distinct regions of the metasurface cross section are observed. Regions 1 and 2 correspond, respectively, to the supporting paper and the adhesive layer onto which the MXene was deposited. Region 3 shows MXene itself, and the image in the inset highlights the characteristic layered structure of the 2D material. We observe that the SEM image corresponds to a locally fractured and partially delaminated edge created during sample cutting and, therefore, does not represent the full through-thickness of the paper substrate. At high magnification, the cross section captures only a small torn flap of the paper rather than the intact multilayer structure, which explains why the visible region appears much thinner than its actual measured thickness. According to the SEM and AFM analyses, the MXene film has an average thickness of $t_{MXene} = 13\,\mu$m. The combination of t_{MXene} with R value yielded an estimated mean conductivity of $\sigma_{MXene} = 8.97 \times 10^3$ S/m, which was inserted in our simulations. Thus, the flexible metasurface has a total thickness of $163.6\,\mu$m (MXene + offset + liner), i.e., 316 times smaller than the wavelength at $f = 5.8$ GHz. Additional characterizations of the MXene obtained using the same synthesis route used in this work, including UV–vis spectroscopy, x-ray diffraction (XRD), and SEM images of isolated $Ti_3C_2T_x$ flakes, are reported in Refs. 40 and 41. The UV–vis spectrum confirmed the successful formation of high-quality MXene, while XRD patterns evidenced the complete removal of the A layer from the MAX phase precursor. Additional SEM images of individual flakes demonstrated the effective delamination and complete exfoliation of the material, supporting the structural and morphological reliability of MXene employed.

TABLE I. Summary of geometric parameters.

	f_{res} (GHz)	Λ (mm)	a (mm)	b (mm)	g (mm)
SqRR	3.5	23	21	19	…
SqRR	5.8	14	13	11	…
SRR	5.8; 14.2	14	5.5	3.5	3

The three prototype metasurfaces were used in the experimental setup of Fig. 4, with measurements taken with a vector network analyzer (VNA) from Rohde & Schwarz®, model ZNB20. The VNA calibration was performed to measure across the microwave frequencies ranging from 1 to 17 GHz. Then, two identical pyramidal horn antennas, model BTA 118 from BETA Telecom®—with a flat gain of approximately 12 dBi in the same frequency range—were connected to the VNA using matched cables at ports 1 and 2, allowing transmission measurements through the scattering parameter S_{21}, given in dB. The transmitting and receiving antennas were placed in line of sight to each other, separated by a distance of 1.8 m to ensure measurements in the far-field region for the entire analyzed frequency range. Since the antennas introduce undesired

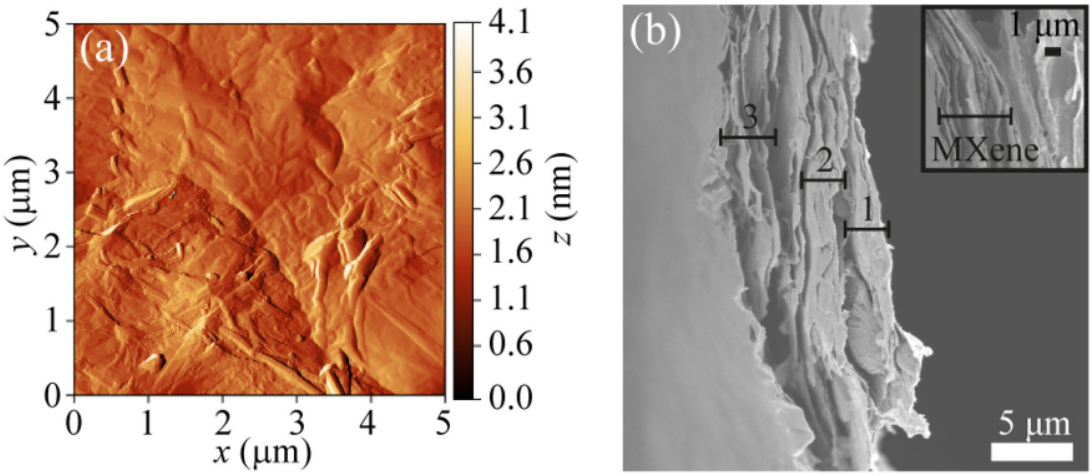

FIG. 3. (a) AFM image of the MXene film deposited onto the adhesive paper and (b) SEM image of the cross section of the metasurface. The inset in (b) confirms the layered characteristic of the MXene film.

effects to S_{21}, we measured S_{21} without the metasurface positioned between the line of sight. Then, the VNA was adjusted to produce a flat $S_{21} = 0$ dB response across the frequency range, effectively compensating for the effects introduced by the antennas after calibration.

Each metasurface was placed between the antennas and surrounded by absorber walls to suppress undesired scattered waves toward the receiving antenna. Nevertheless, since the measurements were performed in the laboratory environment, S_{21} presented ripples in the analyzed frequencies, as noticed in Fig. 5 that shows the transmittances results for all metasurfaces. There is excellent qualitative agreement between the simulated and measured stopband filter responses. As designed and predicted in full-wave simulations (see red-dashed curves), the SqRR metasurfaces presented resonance dips at $f = 3.5$ GHz and $f = 5.8$ GHz in Figs. 5(a) and 5(b), respectively. Since the SqRR unit-cell shapes are symmetric, the spectral response for y-pol and x-pol incident waves are the same. On the other hand, SRR resonances differ for each polarization. As seen in Fig. 5(c), the SRR metasurface exhibited a resonant coupling at $f = 14.2$ GHz for y-pol, while the same SRR metasurface shows resonance at $f = 5.8$ GHz for x-pol waves in Fig. 5(d).

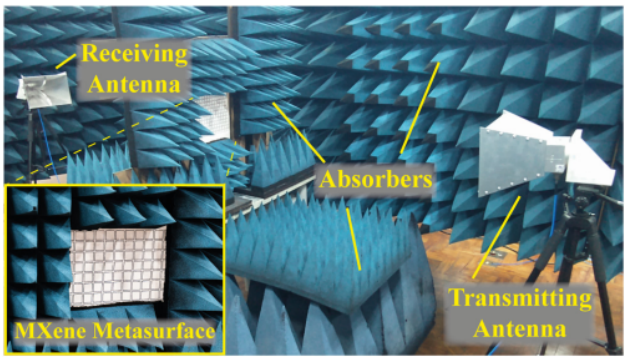

FIG. 4. Experimental setup to measure the MXene-on-paper flexible metasurfaces using a vector network analyzer (VNA) to transmit and receive EM microwave signals through two line-of-sight antennas.

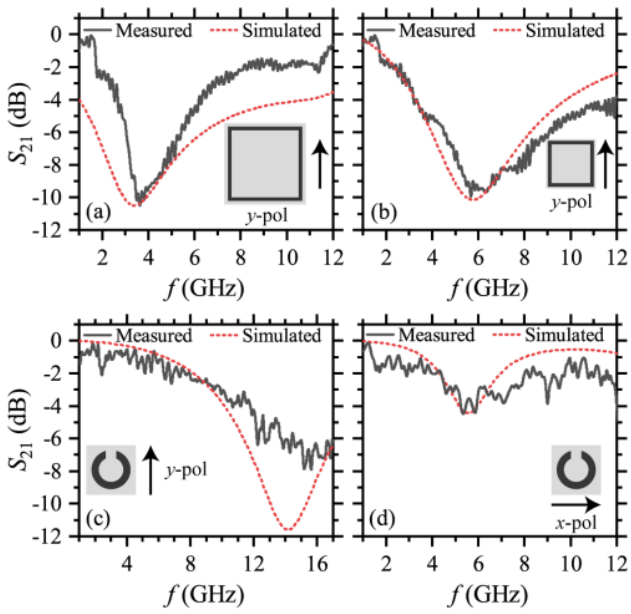

FIG. 5. Comparison between S_{21} simulation and measured results for (a)–(b) SqRR and (c)–(d) SRR unit cells in x-pol and y-pol.

Figure 6 shows the normalized electric (first row) and magnetic (second row) near-field profiles under resonance conditions, where the arrows indicate the LP sense for *y*-pol and *x*-pol. For the SqRR metasurface, the electric field concentration observed in Figs. 6(a) and 6(c) arises mainly from the formation of parallel-plate regions between the horizontal ring segments and the surrounding unit-cell vicinity, producing a strong capacitive effect. A similar behavior is observed in the SRR metasurface, although manifested differently in Figs. 6(e) and 6(g). Under *y*-pol excitation, the resonance is driven by the dipole formed between the two vertical SRR edges, whereas *x*-pol induces a highly localized electric field across the gap, again resembling a capacitive parallel-plate configuration. On the other hand, the magnetic near-field patterns provide complementary insights into the underlying resonance mechanisms. In the SqRR [Figs. 6(b) and 6(d)], the magnetic field is predominantly concentrated along the ring perimeter, indicating a loop-like surface current and a magnetic dipole contribution superimposed on the capacitive electric response. In contrast, the SRR distributions [Figs. 6(f) and 6(h)] exhibit intense magnetic hot-spots inside the loop gap. Specifically, Fig. 6(f) shows that the magnetic field splits into two distinct lobes on opposite sides of the ring, indicating the excitation of a higher-order or hybridized mode that couples more efficiently to the incident higher frequencies, as also observed in Fig. 5(c). In this regime, the magnetic flux circulates in opposite directions along different segments of the ring.

To evaluate the mechanical robustness of the MXene-based metasurface and its suitability for wearable and conformal applications, we performed bending-dependent electromagnetic measurements under three distinct curvature radii. Figure 7 presents the measured transmittance spectra of the four flexible metasurfaces when subjected to different conformal curvatures, namely, the flat (black curves) and three bending radii $r = 284$ mm (red curves), $r = 142$ mm (blue curves), and $r = 95$ mm (green curves), as illustrated in the right-hand panel. Each plot corresponds to one of the metasurfaces comprised by the unit-cell types investigated previously, allowing a direct comparison between their response in planar and bent conditions. As the curvature increases, i.e., as the bending radius decreases, the resonant shape of all metasurfaces exhibits notable modifications, including the increase in the resonance frequency, variations in transmittance depth, and in some cases, a broadening of the spectral response. These discrepancies relative to the flat response arise primarily from the mechanical deformation of the unit cells and the effective change in the local electromagnetic boundary conditions, which jointly perturb the metasurface impedance and coupling mechanisms. The impact of bending is more pronounced for off resonance frequencies, where even small geometric distortions lead to stronger electromagnetic sensitivity [see Figs. 7(a) and 7(b)]. Overall, although the metasurfaces preserve their stopband behavior under deformation, conformal bending introduces measurable deviation in the amplitude and spectral position of their resonances. These results indicate that the paper-based substrate and MXene conductive traces maintain stable electromagnetic behavior under realistic flexible conditions, confirming that the device performance is resilient to mechanical

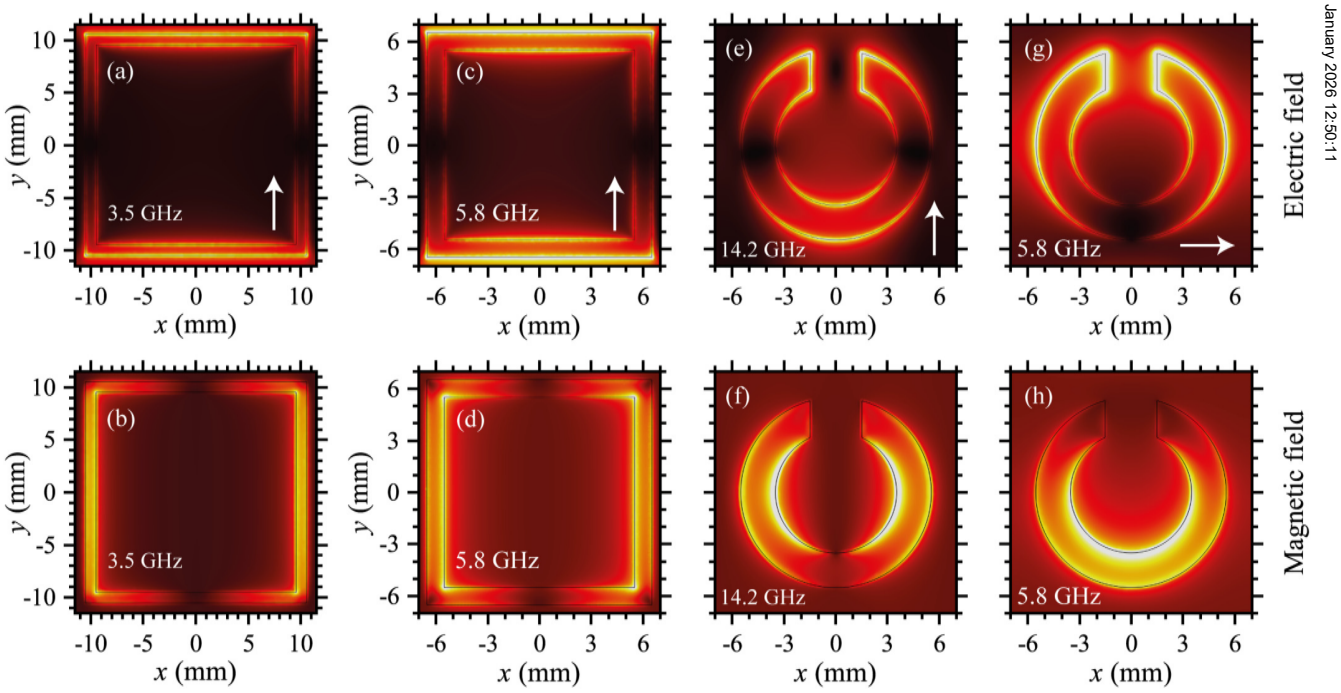

FIG. 6. (a), (c), (e), and (g) show the normalized electric near-field profiles under resonance frequencies, while (b), (d), (f), and (h) present the corresponding normalized magnetic field distributions.

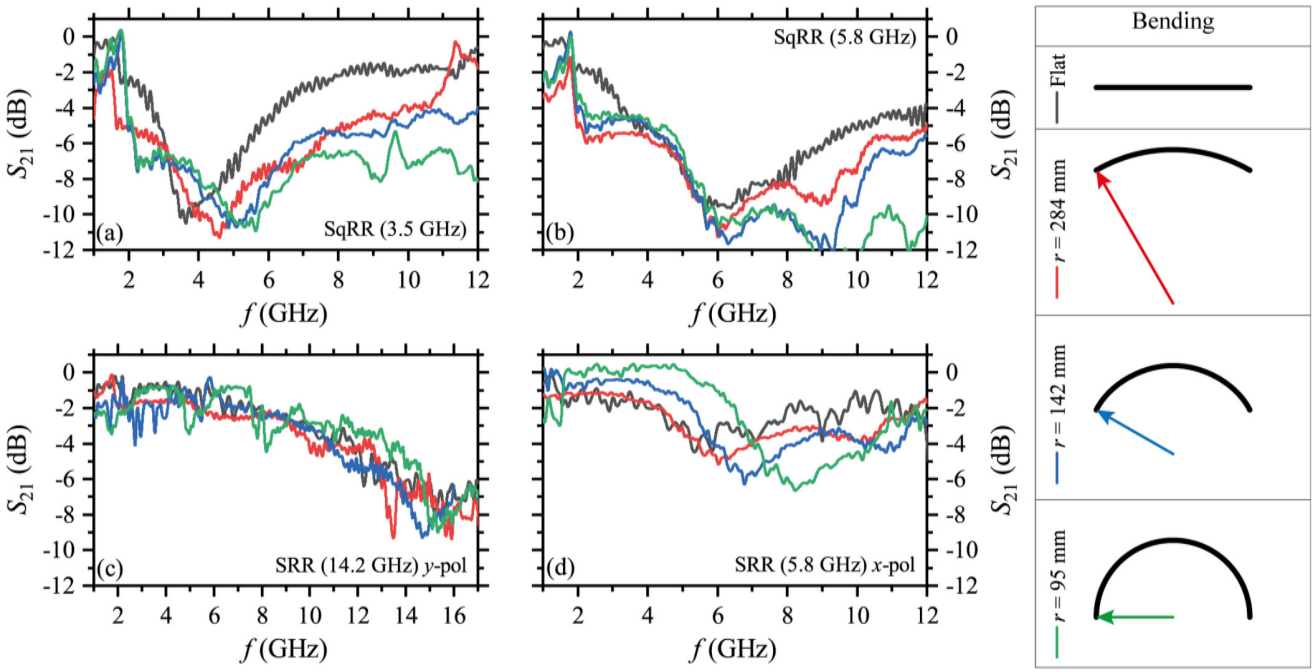

FIG. 7. S_{21} spectra under different conformal curvatures for (a) SqRR (3.5 GHz), (b) SqRR (5.8 GHz), (c) SRR in *y*-pol, and (d) SRR in *x*-pol. The left side panel presents a schematic of the bending radius analyzed, namely, flat (black), $r = 284$ mm (red), $= 142$ mm (blue), and $r = 95$ mm (green).

stress typically encountered in wearable and skin-mounted applications, an important consideration for scenarios requiring stable operation in non-planar or dynamically reconfigurable flexible platforms.

Table II provides a performance comparison between the proposed MXene-based metasurface and previously reported state-of-the-art MXene metasurfaces operating in the microwave regime. The comparison highlights the differences in unit-cell geometry, operating frequency range, substrate type, electrical conductivity, and target applications. Despite employing a paper substrate and moderate conductivity, the present work demonstrates competitive electromagnetic performance, underscoring the practical advantages of the proposed approach in terms of flexibility and cost.

Despite the qualitative agreement between experiments and simulations, the resonance dips are higher than $S_{21}^{res} = -12$ dB for all cases. It means that the prototypes had low wave coupling levels compared with the conventional metallic materials. The main reason is associated with the low MXene electrical conductivity obtained in the synthesis ($\sigma_{MXene} = 8.97 \times 10^3$ S/m), which introduces an additional ohmic loss and contributes to the reduced Q-factor in the measured resonances. For comparison purposes, in Fig. 8, we hypothetically assumed higher σ_{MXene} values to analyze the increase in the coupling strength. We discuss only the SqRR seen in Fig. 5(b), but the phenomena can be extended for other unit-cell shapes. Increasing the conductivity leads to stronger wave coupling, evidenced by the low S_{21}^{res} dip levels in resonance frequency in Fig. 8(a). In the inset, one notes that a MXene dispersion with electrical conductivity at least $\sigma_{MXene} = 10^5$ S/m would be necessary to have resonance levels of $S_{21}^{res} < -20$ dB.

Remarkably, σ_{MXene} increase does not change the metasurface resonance properties, as seen in Fig. 8(b). The blue inverted triangles are for resonance frequencies f_{res} (left *y* axis), while the red triangles are for the S_{21} minimum dip in the f_{res} (right *y*-axis). The resonance remains unaltered for all hypothesized σ_{MXene}—with a

TABLE II. Performance comparison with existing state-of-the-art microwave MXene metasurfaces.

Reference	Unit cell	Freq.	Substr.	σ_{MXene}	Contribution
24	Digitally coded	2–20 (GHz)	PEDOT:PSS	2×10^4 (S/m)	Origami/Kirigami absorbers
25	SRR	2–12 (GHz)	Acetate	10^4 (S/cm)	Kirigami selective surfaces
42	Dual SRR	3–5 (GHz)	Rigid Rogers 4350	5.8×10^5 (S/cm)	EMI shielding
43	Film	8.2–12.4 (GHz)	Rigid borosilicate glass	1.32×10^6 (S/m)	EMI shielding
This work	SqRR; SRR	2–17 (GHz)	Flexible paper	8.97×10^3 (S/m)	Wearable wireless devices

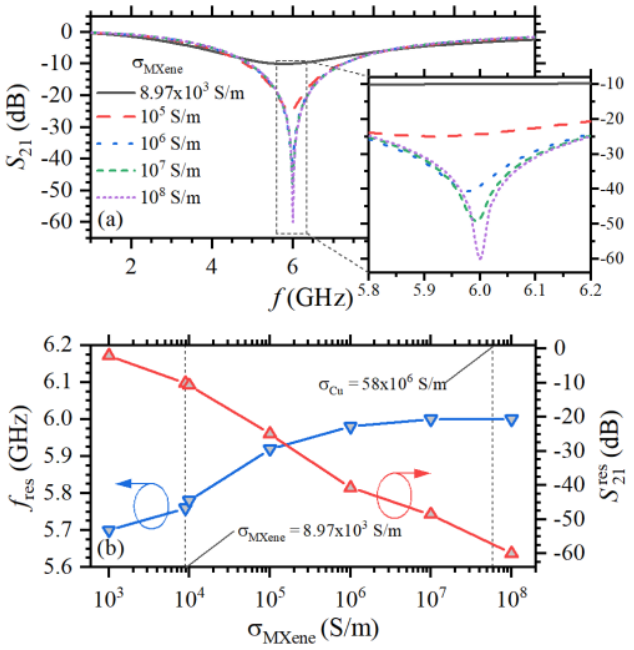

FIG. 8. (a) S_{21} spectra under different MXene electrical conductivities and (b) respective f_{res} (blue) and S_{21}^{res} (red).

slight resonance displaced toward to $f_{res} = 6$ GHz—and a quasi-linear S_{21}^{res} decrease with each successive increase in electrical conductivity by an order of magnitude. These resonance shifts can be minimized through careful geometric optimization or compensation strategies, ensuring stable band positioning even at higher conductivities. The key point highlighted here is that MXene-based patterns remain capable of supporting well-defined resonances whose quality systematically improves as the film conductivity increases. In comparison with conventional copper layers ($\sigma_{Cu} = 5.8 \times 10^7$ S/m), MXene presents a potential solution as a conductive component for flexible metasurfaces. Obviously, this requires optimization of MXene ink formulation and deposition, not to outperform metals in absolute terms, but to enhance the electromagnetic performance of flexible and paper-based MXene microwave metasurfaces.

IV. CONCLUSION

This study introduced a novel flexible metasurface comprised of MXene dispersion deposited on a paper-based substrate. The proposal used an easy and inexpensive fabrication method by depositing MXene dispersion onto adhesive labels, with the top sheet working as the deposition mask outlined with the unit-cell pattern through a cutter printer and the bottom sheet as the substrate. AFM and SEM analyses confirmed the presence of 2D MXene and paper layers, indicating that the total thickness of the structure is 316 times smaller than the wavelength at the resonant frequency at $f = 5.8$ GHz. The EM spectral responses agreed qualitatively with full-wave simulations for all designed unit-cell shapes, but the results indicate that improvements on MXene synthesis are required for better resonance coupling. Furthermore, EM responses suggest that the materials used are promising candidates for flexible devices in health monitoring and dynamic wireless communication applications.

ACKNOWLEDGMENTS

This work was funded by the following research projects: Brasil 6G Project with support from RNP/MCTI (Grant No. 01245.010604/2020-14), xGMobile Project code XGM-AFCCT-2024-7-9-1 with resources from EMBRAPII/MCTI (Grant No. 052/2023 PPI IoT/Manufatura 4.0 and FAPEMIG Grant No. PPE-00124-23), SEMEAR Project supported by FAPESP (Grant No. 22/09319-9), SAMURAI Project supported by FAPESP (Grant No. 20/05127-2), Ciência por Elas with resources from FAPEMIG (Grant No. APQ-04523-23), Fomento à Internacionalização das ICTMGs with resources from FAPEMIG (Grant No. APQ-05305-23), and INEO (FAPESP 2025/27044-5). We also acknowledge the financial support from the Brazilian agency National Council for Scientific and Technological Development-CNPq (Nos. 308068/2025-4 and 405014/2025-2) and FAPESP (No. 2018/22214-6).

AUTHOR DECLARATIONS

Conflict of Interest

The authors have no conflicts to disclose.

Author Contributions

William O. F. Carvalho: Data curation (equal); Formal analysis (equal); Methodology (equal); Project administration (equal); Software (equal); Validation (equal); Visualization (equal); Writing – original draft (equal); Writing – review & editing (equal). **Murilo H. M. Facure:** Data curation (equal); Formal analysis (equal); Investigation (equal); Methodology (equal); Validation (equal); Visualization (equal); Writing – original draft (equal). **Luciano Leonel Mendes:** Project administration (equal); Resources (equal); Writing – review & editing (equal). **Osvaldo N. Oliveira Jr.:** Writing – review & editing (equal). **Daniel S. Correa:** Data curation (equal); Supervision (equal); Writing – review & editing (equal). **Jorge Ricardo Mejía-Salazar:** Conceptualization (equal); Supervision (equal); Writing – review & editing (equal).

DATA AVAILABILITY

The data that support the findings of this study are available from the corresponding author upon reasonable request.

REFERENCES

[1]J. Huang, T.-K. Wu, and S.-W. Lee, "Tri-band frequency selective surface with circular ring elements," IEEE Trans. Antennas Propag. **42**, 166–175 (1994).
[2]R. Mittra, C. H. Chan, and T. Cwik, "Techniques for analyzing frequency selective surfaces—A review," Proc. IEEE **76**, 1593–1615 (1988).
[3]H. Jeong, Y. Yang, H. Cho, T. Badloe, I. Kim, R.-M. Ma, and J. Rho, "Emerging advanced metasurfaces: Alternatives to conventional bulk optical devices," Microelectron. Eng. **220**, 111146 (2020).

[4]G. Cao, H.-X. Xu, L.-M. Zhou, Y. Deng, Y. Zeng, S. Dong, Q. Zhang, Y. Li, H. Yang, Q. Song, X. Liu, Y. Li, and C.-W. Qiu, "Infrared metasurface-enabled compact polarization nanodevices," Mater. Today **50**, 499–515 (2021).
[5]C. Chen, K. Kaj, X. Zhao, Y. Huang, R. D. Averitt, and X. Zhang, "On-demand terahertz surface wave generation with microelectromechanical-system-based metasurface," Optica **9**, 17–25 (2022).
[6]T. Gu, H. J. Kim, C. Rivero-Baleine, and J. Hu, "Reconfigurable metasurfaces towards commercial success," Nat. Photon. **17**, 48–58 (2023).
[7]H.-T. Chen, A. J. Taylor, and N. Yu, "A review of metasurfaces: Physics and applications," Rep. Prog. Phys. **79**, 076401 (2016).
[8]P. Thureja, R. Sokhoyan, C. U. Hail, J. Sisler, M. Foley, M. Y. Grajower, and H. A. Atwater, "Toward a universal metasurface for optical imaging, communication, and computation," Nanophotonics **11**, 3745–3768 (2022).
[9]F. Bilotti, M. Barbuto, Z. Hamzavi-Zarghani, M. Karamirad, M. Longhi, A. Monti, D. Ramaccia, L. Stefanini, A. Toscano, and S. Vellucci, "Reconfigurable intelligent surfaces as the key-enabling technology for smart electromagnetic environments," Adv. Phys.: X **9**, 2299543 (2024).
[10]J. R. Reis, M. Vala, and R. F. S. Caldeirinha, "Review paper on transmitarray antennas," IEEE Access **7**, 94171–94188 (2019).
[11]B. Ferreira Gomes, A. U. Zaman, and J. R. Mejía-Salazar, "All-metallic-metasurface-based wideband dual Fabry–Pérot resonance antenna array with high directivity and polarization purity," IEEE Trans. Antennas Propag. **73**, 3692–3703 (2025).
[12]M. L. Tseng, Y. Jahani, A. Leitis, and H. Altug, "Dielectric metasurfaces enabling advanced optical biosensors," ACS Photon. **8**, 47–60 (2021).
[13]M. Iwanaga, T. Hironaka, N. Ikeda, T. Sugasawa, and K. Takekoshi, "Metasurface biosensors enabling single-molecule sensing of cell-free DNA," Nano Lett. **23**, 5755–5761 (2023).
[14]Z. Zhang, R. Zhao, M. Cong, and J. Qiu, "Developments of terahertz metasurface biosensors: A literature review," Nanotechnol. Rev. **13**, 20230182 (2024).
[15]Y. Guo, X. Lv, C. Li, X. Wu, X. Wang, J. Wang, and K. Bi, "Double-layered ceramic disk-constructed all-dielectric Huygens metasurface perfect absorber," IEEE Trans. Antennas Propag. **72**, 6801–6806 (2024).
[16]K. N. Paracha, S. K. A. Rahim, P. J. Soh, and M. Khalily, "Wearable antennas: A review of materials, structures, and innovative features for autonomous communication and sensing," IEEE Access **7**, 56694–56712 (2019).
[17]R. S. Anwar, L. Mao, and H. Ning, "Frequency selective surfaces: A review," Appl. Sci. **8**, 1689 (2018).
[18]X. Hao, Y. Chen, M. Liu, X. Min, X. Cheng, Q. Wang, Q. Xu, X. Zhang, and J. Han, "Recent advances in terahertz manipulations using C-shape-split-ring-resonator metasurfaces," Adv. Opt. Mater. **12**, 2302975 (2024).
[19]S. A. Haque, M. Islam, I. Hossain, F. Alorifi, Z. A. Shamsan, K. Almuhanna, S. K. A. Rahim, and M. Samsuzzaman, "Left-handed metamaterial based on circular split ring (CSRR) resonator for microwave sensing application," Opt. Mater. **152**, 115480 (2024).
[20]E. M. Materón, H. R. D. Filgueiras, E. C. Vilas Boas, F. R. Gómez, F. R. P. Cavalcanti, Y. C. B. Silva, J. Cerqueira, S. Arismar, F. A. P. de Figueiredo, L. L. Mendes, J. Oliveira, N. Osvaldo, and J. R. Mejía-Salazar, "Flexible metasurfaces as sub-6 GHz frequency selective surfaces for 5G applications," J. Appl. Phys. **134**, 145304 (2023).
[21]P. Li, K. Gao, R. Ma, K. Pan, D. Li, F. Liu, P. Li, X. Gan, J. Zhao, and D. Wen, "Stretchable plasmonic metasurfaces for deformation monitoring," Nanophotonics **13**, 4483–4490 (2024).
[22]Y. Zhou, S. Wang, J. Yin, J. Wang, F. Manshaii, X. Xiao, T. Zhang, H. Bao, S. Jiang, and J. Chen, "Flexible metasurfaces for multifunctional interfaces," ACS Nano **18**, 2685–2707 (2024).
[23]F. Li, T. Pan, W. Li, Z. Peng, D. Guo, X. Jia, T. Hu, L. Wang, W. Wang, M. Gao, G. Yao, L. Zuo, M. Bi, X. Weng, W. Tang, and Y. Lin, "Flexible intelligent microwave metasurface with shape-guided adaptive programming," Nat. Commun. **16**, 3161 (2025).
[24]C. Li, G. Wang, M. Peng, C. Liu, T. Feng, Y. Wang, and F. Qin, "Reconfigurable Origami/Kirigami metamaterial absorbers developed by fast inverse design and low-concentration MXene inks," ACS Appl. Mater. Interfaces **16**, 42448–42460 (2024).
[25]O. Niksan, L. Bi, Y. Gogotsi, and M. H. Zarifi, "MXene-based Kirigami designs: Showcasing reconfigurable frequency selectivity in microwave regime," Nat. Commun. **15**, 7793 (2024).
[26]Y.-Z. Zhang, J. K. El-Demellawi, Q. Jiang, G. Ge, H. Liang, K. Lee, X. Dong, and H. N. Alshareef, "MXene hydrogels: Fundamentals and applications," Chem. Soc. Rev. **49**, 7229–7251 (2020).
[27]R. Li, Y. Zhou, Y. Chen, L. Zhou, Y. Yang, J. Xiao, G. L. Liu, J. Wang, L. Huang, and Y. Li, "High-electron-mobility MXene-enhanced metasurface biosensors integrated with microfluidics for real-time multifunctional monitoring," ACS Nano **19**, 12007–12020 (2025).
[28]H. Kim and H. N. Alshareef, "MXetronics: MXene-enabled electronic and photonic devices," ACS Mater. Lett. **2**, 55–70 (2020).
[29]L. Kabir, J. Qi, K. Wijaya, S. Sagadevan, C.-M. Yoon, K. Ullah, and W.-C. Oh, "Recent advances and latest technologies in energy storage applications based on 2D MXene," J. Energy Storage **80**, 110335 (2024).
[30]M.-Y. Qi, W.-Y. Xiao, M. Conte, Z.-R. Tang, and Y.-J. Xu, "Interfacial synergy of Ni single atom/clusters and MXene enabling semiconductor quantum dots based superior photoredox catalysis," ACS Catal. **15**, 129–138 (2025).
[31]Y. Pei, X. Zhang, Z. Hui, J. Zhou, X. Huang, G. Sun, and W. Huang, "$Ti_3C_2T_x$ MXene for sensing applications: Recent progress, design principles, and future perspectives," ACS Nano **15**, 3996–4017 (2021).
[32]F. Shahzad, M. Alhabeb, C. B. Hatter, B. Anasori, S. Man Hong, C. M. Koo, and Y. Gogotsi, "Electromagnetic interference shielding with 2D transition metal carbides (MXenes)," Science **353**, 1137–1140 (2016).
[33]Y. Pei, J. An, K. Wang, Z. Hui, X. Zhang, H. Pan, J. Zhou, and G. Sun, "$Ti_3C_2T_x$ MXene ink direct writing flexible sensors for disposable paper toys," Small **19**, 2301884 (2023).
[34]Y.-Z. Zhang, Y. Wang, Q. Jiang, J. K. El-Demellawi, H. Kim, and H. N. Alshareef, "MXene printing and patterned coating for device applications," Adv. Mater. **32**, 1908486 (2020).
[35]I. Ali, M. Faraz Ud Din, and Z.-G. Gu, "MXenes thin films: From fabrication to their applications," Molecules **27**, 4925 (2022).
[36]M. Q. Mehmood, A. R. Shah, M. A. Naveed, N. Mahmood, M. Zubair, and Y. Massoud, "MXene-based polarization-insensitive UV-VIS-NIR meta-absorber," IEEE Access **11**, 130287–130295 (2023).
[37]X.-X. Wang, H.-T. Wu, W.-S. Wang, Y. Luo, and Y.-J. Zheng, "Ti_3C_2 MXenes meta-film switching ultra-broadband and high-efficiency green EMI shielding," Carbon **213**, 118267 (2023).
[38]S. Nouseen and M. Pumera, "MXene 3D/4D printing: Ink formulation and electrochemical energy storage applications," Adv. Funct. Mater. **35**, 2421987 (2025).
[39]M. H. M. Facure, K. Matthews, R. Wang, R. W. Lord, D. S. Correa, and Y. Gogotsi, "Pillaring effect of nanodiamonds and expanded voltage window of $Ti_3C_2T_x$ supercapacitors in $AlCl_3$ electrolyte," Energy Storage Mater. **61**, 102919 (2023).
[40]M. H. M. Facure, L. A. Mercante, Y. Gogotsi, and D. S. Correa, "ZnO–Co_3O_4 nanofibers/MXene composite with peroxidase-like activity for ascorbic acid detection," ACS Appl. Nano Mater. **8**, 4291–4299 (2025).
[41]M. H. M. Facure, B. S. Sampaio, L. A. Mercante, and D. S. Correa, "The beneficial impact of MXene on the electrochemical performance of graphene quantum dots for dopamine detection," Mater. Today Commun. **42**, 111197 (2025).
[42]Z. Ullah, M. Al Hasan, and I. B. Mabrouk, "EMI shielding for 5G IOT devices with MXene metamaterial absorber," in *2022 9th International Conference on Internet of Things: Systems, Management and Security (IOTSMS)* (IEEE, 2022), pp. 1–4.
[43]R. Rakhmanov, C. E. Shuck, J. Al Hourani, S. Ippolito, Y. Gogotsi, and G. Friedman, "Ultrathin MXene film interaction with electromagnetic radiation in the microwave range," Appl. Phys. Lett. **123**, 204105 (2023).